

A high-temperature acoustic field measurement and analysis system for determining cavitation intensity in ultrasonically solidified metallic alloys

Nanxuan Xu^a, Yang Yu^b, Wei Zhai^a, Jianyuan Wang^{a,*}, Bingbo Wei^a

^a School of Physical Science and Technology, Northwestern Polytechnical University, Xi'an 710129, People's Republic of China

^b School of Marine Science and Technology, Northwestern Polytechnical University, Xi'an 710129, People's Republic of China

ARTICLE INFO

Keywords:

High-temperature acoustic field measurement
Transient cavitation
Stable cavitation
Ultrasonic solidification

ABSTRACT

A high-temperature acoustic field measurement and analysis system (HTAFS) was self-designed and developed to achieve real-time acoustic field analysis and quantitative cavitation characterization within high-temperature liquids. The acoustic signal was acquired by a high-temperature resistant waveguide and calibrated by separate compensation of line and continuous spectra to eliminate frequency offsets. Moreover, a new method was proposed to derive from the continuous-spectrum sound intensity and line-spectrum sound intensity in the frequency band above 1.5 times the fundamental frequency to characterize the intensity of transient cavitation and stable cavitation. The acoustic field characteristics within solidifying liquid Al-7 %Si alloy were successfully determined by this system. With the increase of ultrasound amplitude, the acoustic pressure in the alloy melt increased to be stable, the transient cavitation intensity first rose and then declined, and the stable cavitation intensity remained unchanged. Combined with the structural evolution of the primary $\alpha(\text{Al})$ phase, the transient cavitation intensity was determined to be the dominant factor for the ultrasound-induced grain refinement effect.

1. Introduction

Ultrasonic cavitation is a complex nonlinear physical phenomenon that arouses intensive research interest [1-5]. When power ultrasound propagates through a liquid, the cavitation bubble oscillates under the alternating action of positive and negative pressure, corresponding to stable cavitation. If the positive pressure is strong enough, cavitation bubbles collapse to induce transient cavitation [6,7], which results in local ultrahigh temperature and pressure, as well as micro-jet when the bubble is next to the surface [8,9]. To reveal the underlying cavitation mechanism, direct observation methods [10-12], chemical methods [13,14], optical methods [15], and acoustic methods [16-18] have been applied, among which the acoustic method can quantitatively analyze and characterize cavitation intensity by using sensors to receive acoustic signals from the cavitation field. The typical cavitation noise spectrum shows the form of a series of line spectra overlapped on a continuous spectrum [19,20]. The continuous spectrum stands for transient cavitation [9,16,21,22], while the line spectra reflect the dynamic characteristics of stable cavitation [17,23]. However, its compositions are complex [24]: in addition to the direct field, cavitation bubbles and linearly pulsating bubbles can also oscillate at a fundamental frequency

f_0 and emit a fundamental acoustic signal; nonlinear oscillations of bubbles [25], as well as large amplitude nonlinear vibration of transducer and waveform distortion in nonlinear acoustic wave propagation, can cause harmonic nf_0 ; the subharmonic $0.5f_0$ and ultraharmonic $(n + 0.5)f_0$ peaks attributed to the combined effects of period doubling [26], subharmonic oscillations [27], chaotic oscillations and microjet emission [28].

However, limited by the Curie temperature of piezoelectric ceramic chips, general commercial acoustic sensors cannot operate in high-temperature environments, which hampers the wide application and development of power ultrasound technology in various fields. For example, the lack of high-temperature acoustic field information within solidifying alloy makes it impossible to establish quantitative relation between acoustic field and microstructure evolution and thereby constrains the modulation effect of power ultrasound on metallic alloy solidification. Currently, there have been some reports on the high-temperature acoustic field measurement, and the main idea is to transfer the acoustic signal in high-temperature liquids by using heat-resisting waveguide rods. T. Matsunaga et al. [29] employed a waveguide rod with high-temperature resistance and a digital oscilloscope to form a cavitometer and used the specific frequencies of 5, 10, and 260

* Corresponding author.

E-mail address: wangjy@nwpu.edu.cn (J. Wang).

<https://doi.org/10.1016/j.ultsonch.2023.106343>

Received 27 December 2022; Received in revised form 6 February 2023; Accepted 20 February 2023

Available online 23 February 2023

1350-4177/© 2023 The Authors. Published by Elsevier B.V. This is an open access article under the CC BY-NC-ND license (<http://creativecommons.org/licenses/by-nc-nd/4.0/>).

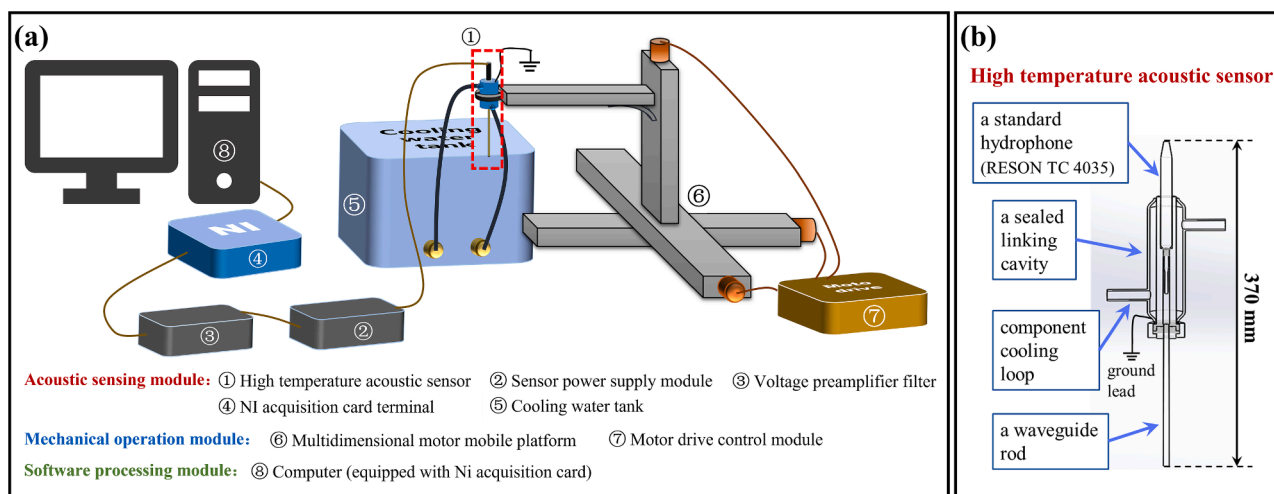


Fig. 1. The high-temperature acoustic field measurement and analysis system: (a) system components; (b) structural schematic of the high temperature acoustic field sensor.

Table 2.1 Technical parameters of high-temperature acoustic field measurement and analysis system.

Parameter	Value
Operating temperature range	273–1873 K
Measurement frequency range	10–800 kHz
RESON TC4035 sensitivity	-214 dB ± 2 dB re 1 V/μ Pa (at 100 kHz, room temperature)
Maximum sampling rate	3.571 MS/s
Gain settings	0–10–20–30–40–50 ± 1 dB
Storage space	4 TB

kHz to characterize the cavitation strength of aluminum alloys. S. Komarov et al. [30] developed a high-temperature cavitometer based on a similar configuration and proposed a method to integrate the energy in four different frequency bands in 0.3–10 MHz frequency range. However, there was no calibration process to ensure the accuracy, and the measured quantities were in the form of the electrical signal of voltage, lacking clear physical meaning. I. Tzanakis et al. [31] first realized the calibration by employing a particular acoustic source that emitted a

special driving waveform, which was difficult to operate with relatively low efficiency. Meanwhile, the acoustic pressure was selected to characterize the total cavitation intensity of pure aluminum melt without distinguishing stable and transient cavitation.

To tackle the above issues, a high-temperature acoustic field measurement and analysis system (HTAFS) is elaborately designed and developed in this work. The HTAFS realizes the acquisition, real-time processing, and storage management of cavitation noise in high-temperature liquids, and an effective characterization method for distinguishing stable cavitation and transient cavitation is presented. By using the HTAFS, the acoustic field variation during the dynamic solidification of liquid Al-7%Si alloy was in-situ measured and analyzed to establish the relationship between acoustic field and solidification microstructures.

2. Description of HTAFS

2.1. System components

As shown in Fig. 1(a), the self-developed HTAFS mainly consists of acoustic sensing module, mechanical operation module, and software processing module, whose technical parameters are shown in Table 2-1.

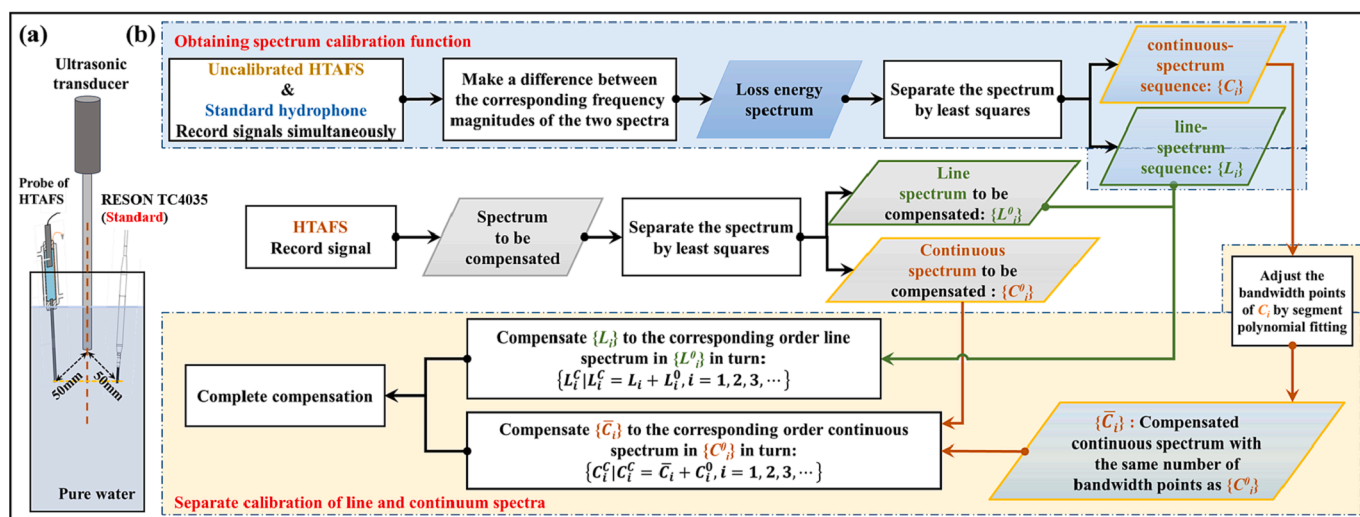


Fig. 2. Line and continuous spectra separation calibration process for HTAFS: (a) location of the HTAFS probe and the standard hydrophone during calibration; (b) calibration flow chart.

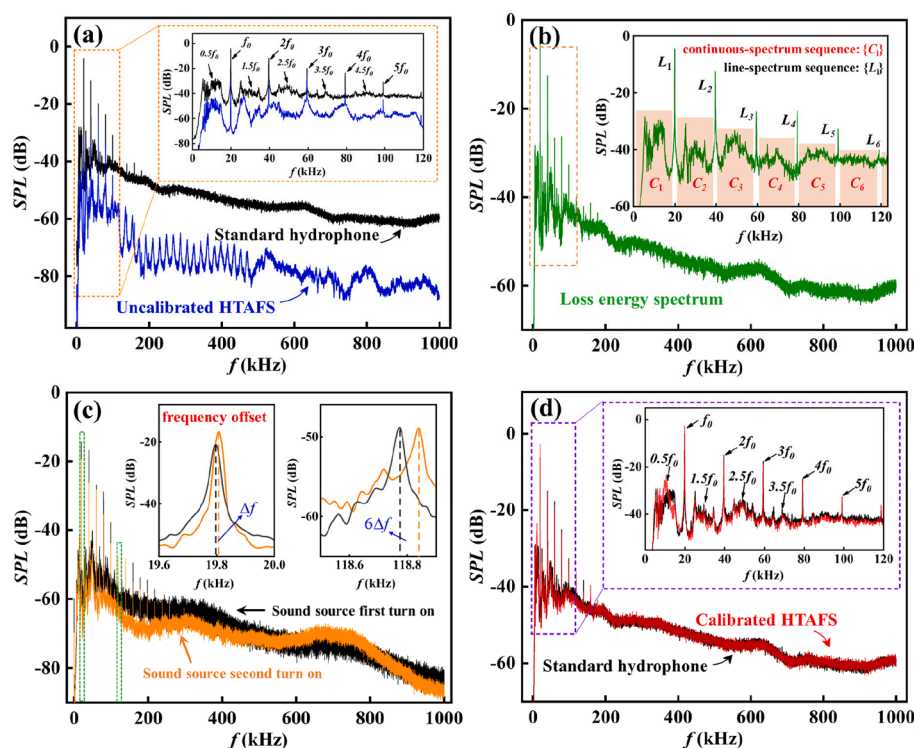


Fig. 3. Spectra during HTAFS calibration: (a) cavitation noise spectra measured by uncalibrated HTAFS and the standard hydrophone under the same condition. The inset shows the amplification of the two spectra in 0–120 kHz bandwidth; (b) the loss energy spectrum in 0–1000 kHz. The inset illustrates the amplification in the 0–120 kHz bandwidth and the compensation continuous spectrum sequence $\{C_i\}$ and the line spectrum sequence $\{L_i\}$; (c) the frequency offset generated under different start-ups. The two insets show the frequency offset at the driving frequency and at the 6th harmonic; (d) comparison of noise spectra measured by calibrated HTAFS and the standard hydrophone. The inset enlarges the compensation details covering 0–120 kHz bandwidth.

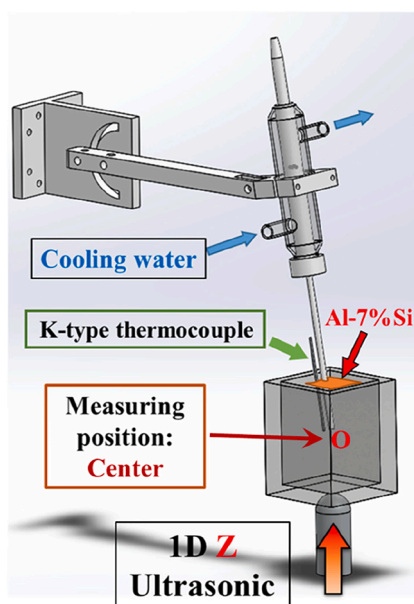


Fig. 4. Experimental process of measuring the internal sound field in liquid Al-7%Si alloy.

The acoustic sensing module is composed of high-temperature acoustic sensor, sensor power supply unit, voltage preamplifier filter (VP2000, RESON), high-speed AD acquisition card (PCIe-6374, NI), and sensor cooling water tank. As a critical component, the high-temperature acoustic sensor is made up of a standard hydrophone (TC4035, RESON), a sealed linking cavity, and a 5 mm diameter waveguide rod made of quartz or ceramic, as shown in Fig. 1(b). The linking cavity is referred to the structure of the condenser, which is divided into two isolated layers: the inner layer is a 10 mm diameter conduction chamber filled with pure water to connect the waveguide rod and the RESON

TC4035 hydrophone probe, and the outer layer is a 5 mm thick cooling layer that is connected to a recirculating cooling water tank. This design protects the sensor from heat sources and makes sure it works at room temperature. During the operation of the acoustic sensing module, the acoustic signal is acquired by the waveguide rod to pure water in the sealed link cavity, then transformed into an electrical signal by a standard hydrophone. After filtering and amplification, the signal is converted to a digital signal by a high-speed AD acquisition card for subsequent processing.

The mechanical operation module is composed of multidimensional motor mobile platform and motor drive control unit, which can drive the high-temperature acoustic sensor to achieve three-dimensional spatial positioning with accuracy ≤ 0.2 mm. The software processing module realizes the functions of the parameter setting, acoustic field measurement, calibration, analysis, real-time display, and data storage, which is built with LabVIEW and Matlab. In the experimental measurement process, various cavitation characterization quantities, such as time domain waveform, spectrogram, acoustic pressure, transient cavitation intensity, and stable cavitation intensity within high-temperature liquids, are displayed immediately on the main interface. The system operating settings, such as sampling frequency, acquisition time, space location, FFT parameters, motor drive speed, waveguide rod type, storage path, and so on, are set through the sub-interface. In addition, the built-in database can store the raw signal and processing data for subsequent analysis.

2.2. Frequency domain calibration method

The operation flow for the calibration process of HTAFS was illustrated in Fig. 2, which was carried out at room temperature. Firstly, a VCX1500 ultrasonic transducer with driving frequency $f_0 = 20$ kHz was taken as the calibration source, and its horn was located at the center point of pure water contained in a cube container. The probe of HTAFS and the standard hydrophone (RESON TC4035) were placed symmetrically on both sides of the ultrasonic horn to simultaneously measure the acoustic field, and the results were shown in Fig. 3(a). It is evident

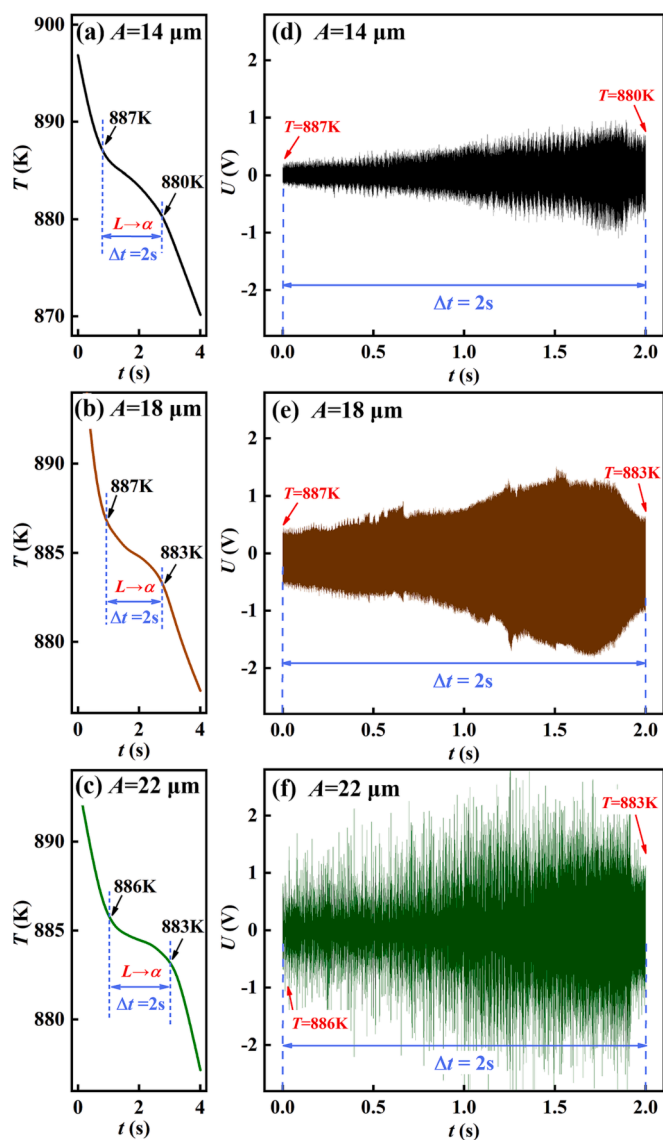


Fig. 5. Solidification curves and the cavitation noise signals measured by HTAFS of the nucleation growth phase of the primary $\alpha(\text{Al})$ phase during the ultrasonic solidification of Al-7 %Si alloy under different ultrasonic conditions: (a, d) $A = 14 \mu\text{m}$; (b, e) $A = 18 \mu\text{m}$; (c, f) $A = 22 \mu\text{m}$.

that the spectrum measured by the uncalibrated HTAFS was significantly smaller than that of the standard hydrophone in the frequency from 0 to 1000 kHz. The energy loss induced by the propagation of ultrasonic waves through the waveguide rod/the linking cavity/the hydrophone interface takes the main responsibility of this amplitude deviation. However, since the measurement process was recorded synchronously under the same ultrasonic source condition, the spectra acquired by the two sensors do not have any frequency offset, which can be observed clearly in the inset of Fig. 3(a). There are significant “sawtooth” fluctuations in the spectrum of the uncalibrated HTAFS, which may be brought about by mechanical vibrations of the waveguide rod [31] or reflections and resonances from signal conduction in the linking cavity. In this case, the loss energy spectrum of the high-temperature acoustic field sensor can be obtained by making the difference between the two spectra at the same frequency, as shown in Fig. 3(b). Because the waveguide rod had good thermal stability and the HTAFS probe was equipped with a cooling circulation system, the working temperature of the sensor was not affected by the temperature of the melt to be measured. Considering the influence of the medium

properties on the acoustic energy coupling into the waveguide, this loss function can be directly applied to compensate for the acoustic signal measured in a high-temperature melt when the acoustic properties of the metallic melt are close to water.

However, due to the sensitivity of inductance and capacitance, differences in frequency matching inevitably occur between the drive power supply and the transducer. Even by using the same ultrasound source transducer during actual determination in high-temperature liquid, there was always a tiny random offset Δf from f_0 at each time (Fig. 3(c)). Since the frequency at the harmonics was an integer multiple of the driving frequency, the frequency offset at the harmonics could be amplified by the same multiple to $n\Delta f$, which can be observed more clearly in the inset of Fig. 3(c). Due to this inevitably random frequency offset, the loss energy spectrum obtained in pure water cannot be directly used in calibrating the measurement results. A new calibration method with separate compensation for the line and continuous spectra was proposed as follows. Initially, the line spectrum of the loss energy spectrum was separated to form the compensation line-spectrum sequence $\{L_i : L_1, L_2, L_3, \dots, L_n\}$. Correspondingly, the continuous spectra between each line spectrum formed the compensation continuous-spectrum sequence $\{C_i : C_1, C_2, C_3, \dots, C_n\}$, as shown in the inset of Fig. 3(b). Next, separating the uncalibrated spectra by the same method to obtain the line spectrum sequence $\{L_i^0\}$ and the continuous spectrum sequence $\{C_i^0\}$. Then the compensation line spectrum sequence $\{L_i\}$ was added to the line spectrum $\{L_i^0\}$ in the corresponding harmonic order, thereby completing the line spectrum calibration. On the other hand, different frequency offset in each harmonic led to a difference in the number of bandwidth points between C_i in the continuous spectrum sequence and the uncalibrated continuous spectrum in the corresponding order. Therefore, the segmented least squares fitting method was used for C_i to obtain a compensated continuous spectrum \tilde{C}_i with the same number of spectrum points as the continuous spectrum $\{C_i^0\}$. Hence, the continuous spectrum calibration was completed by adding \tilde{C}_i to the corresponding frequency magnitude of the uncalibrated continuous spectrum $\{C_i^0\}$. Fig. 3(d) shows the calibrated spectrum in the whole frequency range, and the inset enlarges the compensation details within 0–120 kHz bandwidth. It was evident that the calibrated curve by the high-temperature sensor almost overlapped with that of the standard hydrophone, indicating the deviations in both amplitude and frequency were eliminated. This proved that the calibration method was well suited for the calibration of cavitation meters.

2.3. Cavitation intensity characterization

The cavitation intensity is the energy released from cavitation bubbles per unit time and space [32]. With reference to the physical meaning of sound intensity, the two types of cavitation intensity are characterized using the sound intensity components corresponding to different waveforms excited on the spectrum by transient and stable cavitation, respectively. The continuous-spectrum sound intensity component characterizes the transient cavitation intensity. The line-spectrum intensity component corresponding to harmonics, ultraharmonic, and subharmonics is used as an approximation to characterize the stable cavitation intensity. Due to the complexity of the line spectrum sources, this method has some deviations in quantifying the acoustic field characteristics. However, it can systematically reflect the influence of the cavitation field on ultrasonic solidification, thus helping to establish a quantitative relationship between the cavitation field and the microstructure of ultrasonic solidification. As the low-frequency signal attenuates weakly in the liquid, the noise signal in the low-frequency band collected at the measurement point contains reflected noise from other regions within the melt. The direct field is brought about by the drive of the transducer, which does not directly reflect the intensity of the cavitation. The spectrum below $1.5f_0$ is omitted to ensure that interference from low frequency and direct field energy is

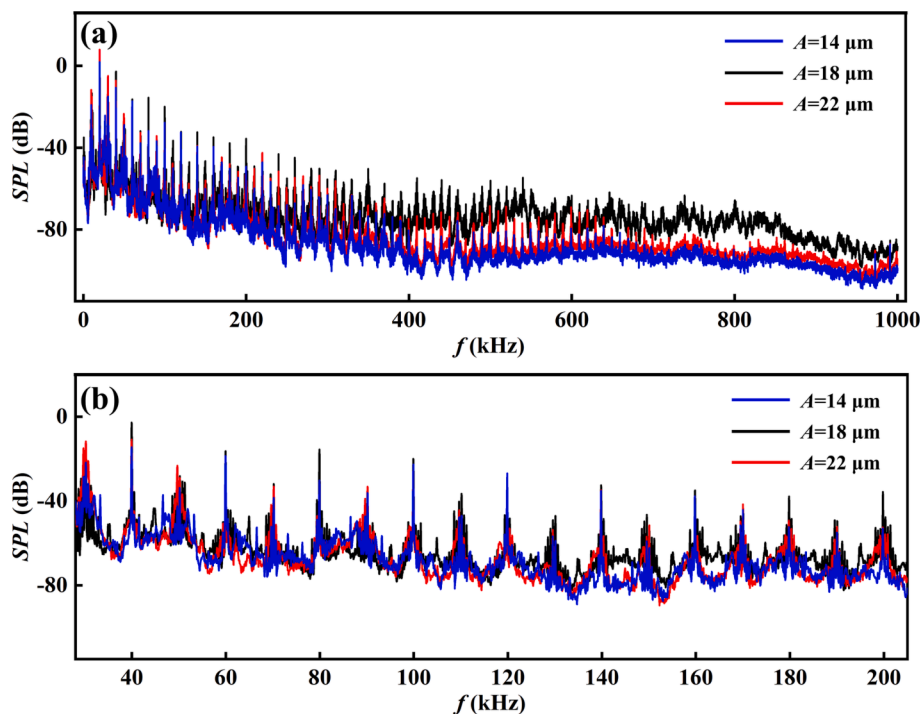


Fig. 6. The spectra measured about 1.7 s after initial nucleation retrieved by the calibrated HTAFS: (a) full frequency band; (b) 30–200 kHz.

eliminated. In addition, the line spectra were all below the frequency of $40f_0$, and the continuous spectrum below $40f_0$ already contained the major energy of transient cavitation. In order to reduce the bandwidth length as much as possible while ensuring that the chosen bandwidth spectrum covered the main cavitation energy, $40f_0$ was finally chosen as the upper bandwidth limit. On this basis, the continuous spectrum sound intensity component (I_t) and the line spectrum sound intensity component (I_s) in the frequency range $1.5f_0$ to $40f_0$ of the cavitation noise are used to characterize the transient cavitation intensity and the stable cavitation intensity, respectively.

The continuous spectrum and line spectrum above the $1.5f_0$ frequency, which are obtained through the least squares separation [33], are denoted as FCS and FLS . The transient cavitation intensity (I_t) and the stable cavitation intensity (I_s) are calculated by Eqs. (1)–(4).

$$SPL_T = 10 \log \sum_{f_i \in FCS} \left[\frac{FCS(f_i)}{M_{FCS}} \right]^2 - L_m - L_r \quad (1)$$

$$SPL_S = 10 \log \sum_{f_i \in FLS} \left[\frac{FLS(f_i)}{M_{FLS}} \right]^2 - L_m - L_r \quad (2)$$

$$I_t = \frac{P_{ref}^2 \times 10^{SPL_T/10}}{\rho c} \quad (3)$$

$$I_s = \frac{P_{ref}^2 \times 10^{SPL_S/10}}{\rho c} \quad (4)$$

where $S_{FCS}(f_i)$ and $S_{FLS}(f_i)$ are the module values of the continuous spectrum and line spectrum; M_{FCS} and M_{FLS} are the bandwidth lengths of the continuous spectrum and line spectrum; SPL_T and SPL_S denote transient cavitation noise sound pressure level and stable cavitation sound pressure level; L_m is the sensor sensitivity, and L_r is the gain of the analog front-end filtering and amplification, both in dB; P_{ref} is the reference acoustic pressure, and the value is $1 \mu\text{Pa}$; ρ is the density of the water, and its value is $1 \times 10^3 \text{ kg/m}^3$; c is the speed of sound in the water, and its value is $1.5 \times 10^3 \text{ m/s}$.

3. Experimental procedure

In order to check the validity of the measurement system and the reliability of the new cavitation characterization quantity, the acoustic field variation during the solidification process of liquid Al-7 %Si alloy was in-situ determined by employing HTAFS. During experiments, the alloy samples were prepared by the raw Al and Si elements equal to or over 99.99 wt% purity and were melted to 1273 K by a high-frequency inductor before being poured into a preheated square graphite casting mold with internal dimensions of $20 \times 20 \times 40 \text{ mm}$. As shown in Fig. 4, a SONICS VCX1500 ultrasonic transducer with a drive frequency of 20 kHz was held upwards by pneumatic cylinders. The ultrasonic waves with amplitudes at 14, 18, and 22 μm were transmitted into the liquid alloy through the bottom wall of the casting mold. The high-temperature sensor of the HTAFS and a K-type NiCr-NiSi thermocouple were inserted in the center of the alloy melt marked point O to measure acoustic and temperature signals based on which the acoustic pressure P , transient cavitation sound intensity I_t and stable cavitation sound intensity I_s were analyzed in real-time. The acoustic measurement process started when the melt was poured into the casting mold until the liquid alloy was completely solidified. Due to the built-in water cooling circulation system in the linking cavity, the change of the alloy melt temperature does not impact the HTAFS measurement. After the experiment, the solidified Al-7 %Si alloy sample was longitudinally sectioned and polished. The microstructure around point O was analyzed by Zeiss Axiovertzoo MAT optical microscope and Image-pro plus software.

4. Results and discussion

Figs. 5(a, b, c) show the cooling curves of the binary Al-7 %Si alloy at 14, 18, and 22 μm ultrasound amplitudes. It can be seen that the solidification of the primary $\alpha(\text{Al})$ phase starts at about 887 K and ends at about 880–883 K. This stage lasts for about 2 s. The cavitation noise signals measured by HTAFS are shown in Figs. 5(d, e, f), whose overall waveforms are in a “horn” shape. Fig. 6 shows the spectra measured about 1.7 s after initial nucleation retrieved by calibrated HTAFS at the maximum value of the time domain spectra magnitude as an example. A

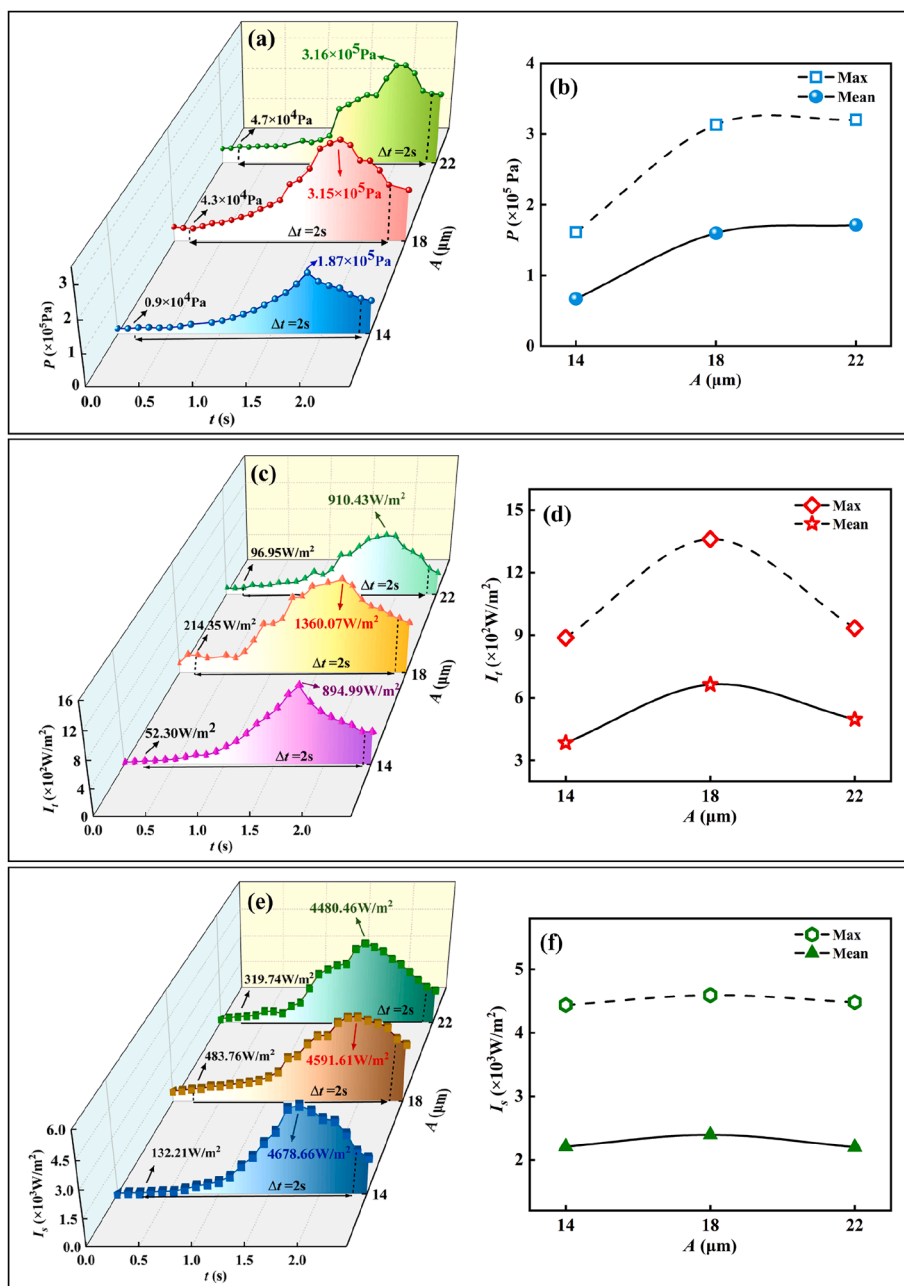


Fig. 7. Measured acoustic fields within solidifying liquid Al-7%Si alloy at different ultrasonic amplitudes: (a) variation of acoustic pressure P with solidification; (b) maximum and average values of acoustic pressure P ; (c) variation of transient cavitation sound intensity I_t with solidification; (d) maximum and average values of transient cavitation sound intensity I_t ; (e) variation of stable cavitation sound intensity I_s with solidification; (f) maximum and average values of stable cavitation sound intensity I_s .

large number of line spectra exist in all the noise spectra. Observing the low frequency band spectra in 0–200 kHz (Fig. 6(b)), it is found that the line and continuous spectrum magnitudes are extremely close among the three ultrasound amplitudes. Once the frequency is greater than 200 kHz, the spectral magnitudes under 18 μm ultrasound amplitude are significantly stronger than those under 14 and 22 μm amplitudes.

Fig. 7 presents the variation of acoustic pressure, transient cavitation intensity, and stable cavitation intensity during the solidification of the primary $\alpha(\text{Al})$ phase. Under each ultrasonic condition, the three physical quantities of P , I_t , and I_s show a trend of first increasing and then decreasing. The mean and maximum values of acoustic pressure under different ultrasonic amplitudes are shown in Fig. 7(b). When the amplitude increases from 14 to 18 μm, the average acoustic pressure P increases from 6.7×10^4 to 1.6×10^5 Pa, and the maximum value increases from 1.6×10^5 Pa to 3.1×10^5 Pa. As sound amplitude increases to 22 μm, the average and maximum values of acoustic pressure inside the melt slightly increase to 1.7×10^5 Pa and 3.2×10^5 Pa. In contrast,

the mean and maximum values of transient cavitation intensity I_t show a completely different trend from that of acoustic pressure. On increasing the ultrasonic amplitude from 14 to 22 μm, the mean value of I_t increases from 3.8×10^2 to 6.6×10^2 W/m² and then decreases to 4.9×10^2 W/m² while the maximum value increases from 8.9×10^2 to 1.4×10^3 W/m², and then decreases again to 9.1×10^2 W/m². Unlike P and I_t , the stable cavitation intensity I_s does not vary significantly at different amplitude conditions, as supported by the results in Fig. 7(f). The mean values remain between 2.2×10^3 and 2.3×10^3 W/m², and the maximum value is also stable at around 4.5×10^3 W/m². Because the final characteristics of the primary $\alpha(\text{Al})$ phase depend on the accumulation of sound field changes throughout its solidification process, these mean values are applied to characterize the variation of ultrasound pressure, stable cavitation intensity, and transient cavitation intensity versus sound amplitude, and further analyze their effects on the growth feature and grain size of the primary $\alpha(\text{Al})$ phase. It also needs to be mentioned that the magnitude of I_s is nearly four times larger than I_t under the same

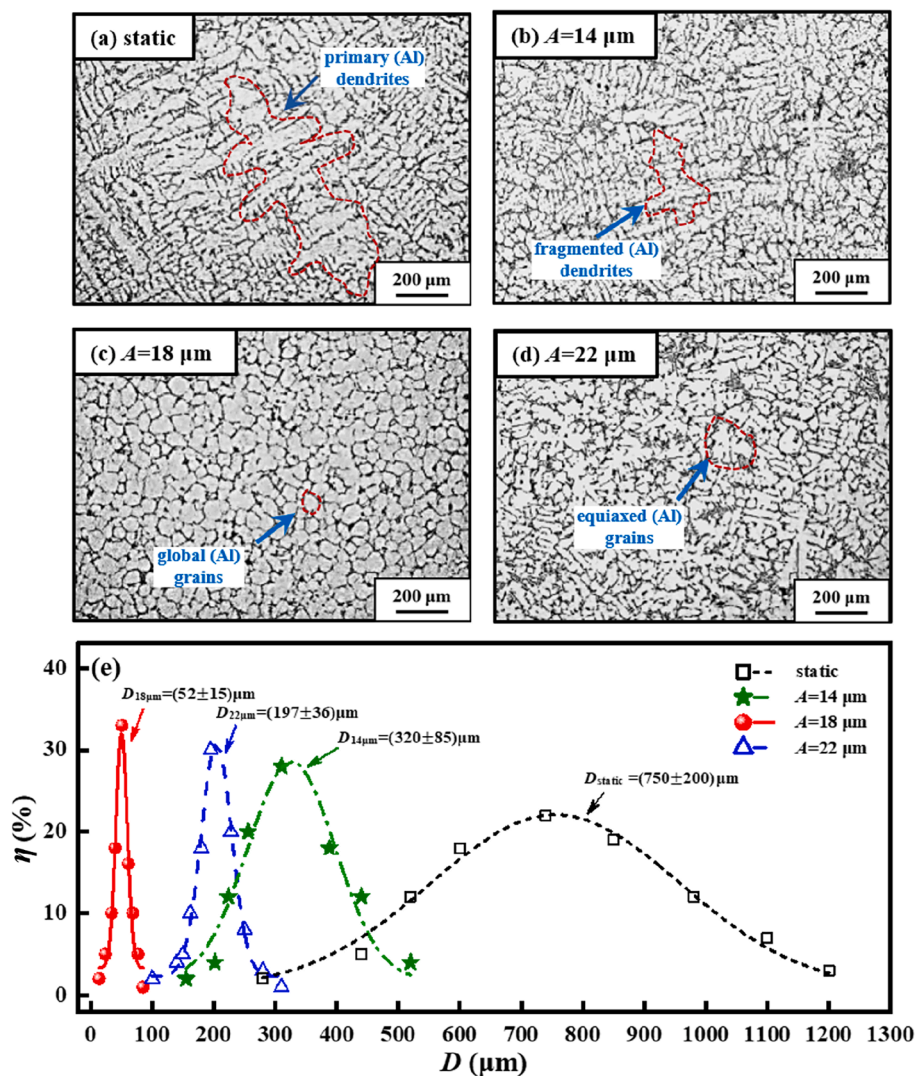


Fig. 8. Microstructure and size distribution of the primary $\alpha(\text{Al})$ phase in solidified Al-7 %Si alloy samples: (a) microstructure under static condition, (b) microstructure formed under $A = 14\ \mu\text{m}$, (c) microstructure formed under $A = 18\ \mu\text{m}$, and (d) microstructure formed under $A = 22\ \mu\text{m}$; (e) size distribution of the primary $\alpha(\text{Al})$ phase. D_{static} , $D_{14\mu\text{m}}$, $D_{18\mu\text{m}}$ and $D_{22\mu\text{m}}$ represent the grain size under different ultrasonic amplitudes of 0, 14, 18, and 22 μm , respectively. η is the distribution probability of size distribution for the primary $\alpha(\text{Al})$ phase.

ultrasonic condition. This suggests that the oscillatory behavior of bubbles is more likely to occur than bubble collapse during the nucleation and growth of the primary $\alpha(\text{Al})$ phase.

Figs. 8(a–d) show the solidification micro-structures of Al-7 %Si hypoeutectic alloy under different ultrasonic conditions. Under static conditions, the primary $\alpha(\text{Al})$ phase develops into very coarse dendrites with secondary dendritic arms. As shown in Fig. 8(e), the primary $\alpha(\text{Al})$ dendrites have a significant deviation in size from each other, whose maximum length is 1200 μm and the average length is 750 μm . At 14 μm ultrasonic amplitude, the primary $\alpha(\text{Al})$ phase becomes fractured dendrites. Once the ultrasound amplitude increases to 18 μm , the primary $\alpha(\text{Al})$ phase grows into a large number of tiny globular grain. At this point, the average size of the grains is 52 μm , and the deviation of the grain size is minimal. The “dendritic-spherical” morphological transformation and size reduction of the primary $\alpha(\text{Al})$ phase grains were also found after the introduction of ultrasound during the solidification of Al-5 %Si [34]. When the ultrasonic amplitude further increases to 22 μm , the primary $\alpha(\text{Al})$ phase showed equiaxed crystals.

Fig. 9 shows the relationship between the average grain size of the primary $\alpha(\text{Al})$ phase D and P , I_s , I_t during the nucleation and growth stage of the primary $\alpha(\text{Al})$ phase based on four sets of replicate experiments. The error bars in the figure are obtained by counting the standard deviation of the data from four repeated experiments, where the longitudinal ones represent the difference in average grain size and the transverse ones represent the difference in acoustic covariance. It can be

found in Fig. 9(a) that the increase of acoustic pressure does not always lead to the reduction of the primary $\alpha(\text{Al})$ grain size, and the nearly identical stable cavitation intensities correspond to two different grain sizes (Fig. 9(b)). These demonstrate that neither acoustic pressure nor stable cavitation intensity is the decisive parameter in ultrasonic grain refining. In contrast, the average grain size of the primary $\alpha(\text{Al})$ phase linearly decreases with the increase of transient cavitation intensity, and the minimum grain size appears under the maximum transient cavitation intensity, as shown in Fig. 9(c), which fully indicates that the transient cavitation intensity is the dominant factor for the ultrasound-induced refinement.

5. Conclusions

- (1) The self-developed HTAFS successfully realizes the high-speed acquisition, the cavitation signal calibration in high-temperature liquids, the analysis and display of acoustic pressure, transient cavitation intensity, and stable cavitation intensity in real-time.
- (2) A new calibration method of frequency domain spectral separation is proposed, in which an ultrasonic transducer with a fixed driving frequency is used as the calibration source, and the high-temperature acoustic field is calibrated separately at the peak frequency point of the line spectrum and the continuous spectrum band.

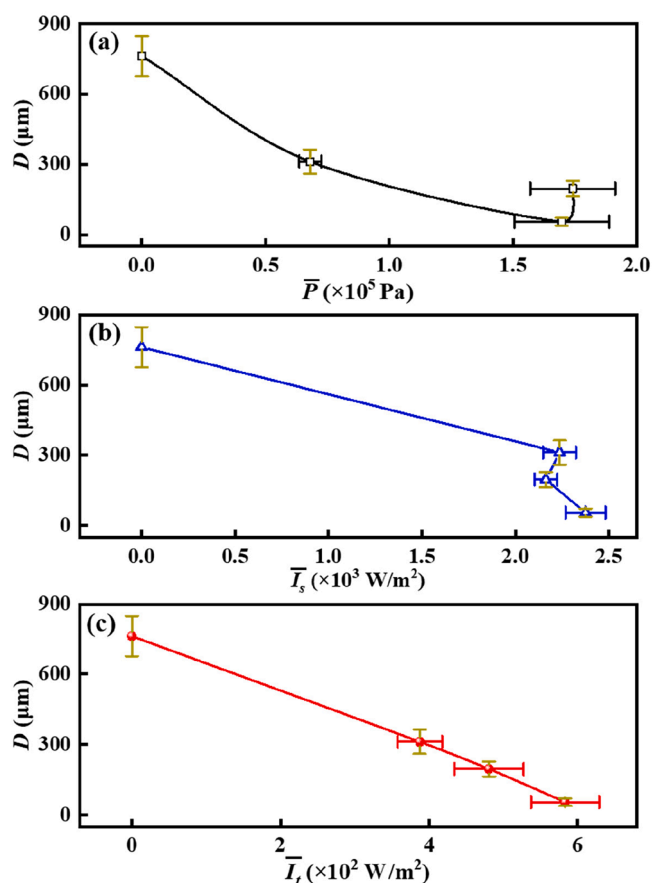


Fig. 9. Relationship between solidification structure and cavitation characterization of Al-7 %Si alloy: (a) grain size of the primary $\alpha(\text{Al})$ phase versus acoustic pressure; (b) grain size of the primary $\alpha(\text{Al})$ phase versus stable cavitation intensity; (c) grain size of the primary $\alpha(\text{Al})$ phase versus transient cavitation intensity.

- (3) The continuous-spectrum sound intensity and the line-spectrum sound intensity of intercepting frequency bands above $1.5f_0$ are used to characterize transient and stable cavitation intensity, which eliminate the interference of the transducer drive energy and the radiated energy of the surrounding in the low-frequency band on the cavitation measurement results.
- (4) The acoustic pressure, stable and transient cavitation intensity are successfully obtained during the solidifying Al-7 %Si alloy, and their relations show that the transient cavitation intensity plays the dominant role in refining primary $\alpha(\text{Al})$ phase, indicating that separate characterization of transient and stable cavitation is vital to reveal the solidification mechanism of liquid alloy within the ultrasonic field.

CRediT authorship contribution statement

Nanxuan Xu: Software, Data curation, Formal analysis, Investigation, Writing – original draft. **Yang Yu:** Methodology, Writing – review & editing. **Wei Zhai:** Investigation, Formal analysis, Project administration, Funding acquisition. **Jianyuan Wang:** Supervision, Writing – review & editing, Validation, Funding acquisition. **Bingbo Wei:** Conceptualization, Resources, Funding acquisition.

Declaration of Competing Interest

The authors declare that they have no known competing financial interests or personal relationships that could have appeared to influence

the work reported in this paper.

Acknowledgement

This work was financially supported by National Natural Science Foundation of China (Nos. 52088101, 52130405, and 51972275), National Key R&D Program of China (2021YFB3502600, 2021YFA0716301), Basic Research Project of Shaanxi Natural Science Foundation (2021JCW-09, 2023-JC-JQ-28), and Key R&D Plan of Shaanxi Province (2020ZDLGY13-03). Useful help from colleagues including Tongtong Jia, Yajie Hu, Ying Zhang and Xu Wang during the experiments and analysis is gratefully acknowledged.

References

- [1] D.G. Eskin, I. Tzanakis, F. Wang, G.S.B. Lebon, T. Subroto, K. Pericleous, J. Mi, Fundamental studies of ultrasonic melt processing, *Ultrason. Sonochem.* 52 (2019) 455–467, <https://doi.org/10.1016/j.ulsonch.2018.12.028>.
- [2] W.H. Wu, P.F. Yang, W. Zhai, B.B. Wei, Oscillation and Migration of Bubbles within Ultrasonic Field, *Chin. Phys. Lett.* 36 (8) (2019), <https://doi.org/10.1088/0256-307X/36/8/084302>.
- [3] C.E. Brennen (Ed.), *Cavitation and Bubble Dynamics*, Cambridge University Press, 2013.
- [4] S. Wang, Q. Wang, R. Chen, Y. Chai, Y. Jin, Y. Su, Improving primary Nbss morphology and fracture toughness in hypoeutectic Nb-Si-Ti ternary alloy by ultrasonic treatment, *Mater. Des.* 212 (2021), 110262, <https://doi.org/10.1016/j.matdes.2021.110262>.
- [5] S. Zhang, H. Kang, M. Cheng, Z. Chen, Z. Wang, E. Guo, J. Li, T. Wang, Ultrasound-Assisted Solidification of a Cu–Cr Alloy, *Acta Metall. Sin. Engl. Lett.* 35 (2022) 2082–2088, <https://doi.org/10.1007/s40195-022-01433-3>.
- [6] H. Wu, H. Zheng, Y.Y. Li, C.D. Ohl, H.X. Yu, D.C. Li, Effects of surface tension on the dynamics of a single micro bubble near a rigid wall in an ultrasonic field, *Ultrason. Sonochem.* 78 (2021) 105735, <https://doi.org/10.1016/j.ulsonch.2021.105735>.
- [7] Q.Y. Zeng, S.R. Gonzalez Avila, C.D. Ohl, Splitting and jetting of cavitation bubbles in thin gaps, *J. Fluid Mech.* 896 (2020) A28, <https://doi.org/10.1017/jfm.2020.356>.
- [8] D.J. Flannigan, K.S. Suslick, Plasma formation and temperature measurement during single-bubble cavitation, *Nature* 434 (2005) 52–55, <https://doi.org/10.1038/nature03361>.
- [9] I. Tzanakis, D.G. Eskin, A. Georgoulas, D.K. Fytanidis, Incubation pit analysis and calculation of the hydrodynamic impact pressure from the implosion of an acoustic cavitation bubble, *Ultrason. Sonochem.* 21 (2014) 866–878, <https://doi.org/10.1016/j.ulsonch.2013.10.003>.
- [10] D. Shu, B. Sun, J. Mi, P.S. Grant, A High-Speed Imaging and Modeling Study of Dendrite Fragmentation Caused by Ultrasonic Cavitation, *Metall. Mater. Trans. A* 43 (2012) 3755–3766, <https://doi.org/10.1007/s11661-012-1188-3>.
- [11] A. Priyadarshi, M. Khavari, S. Bin Shahrani, T. Subroto, L.A. Yusuf, M. Conte, P. Prentice, K. Pericleous, D. Eskin, I. Tzanakis, In-situ observations and acoustic measurements upon fragmentation of free-floating intermetallics under ultrasonic cavitation in water, *Ultrason. Sonochem.* 80 (2021), 105820, <https://doi.org/10.1016/j.ulsonch.2021.105820>.
- [12] F. Wang, D. Eskin, J. Mi, C. Wang, B. Koe, A. King, C. Reinhard, T. Connelly, A synchrotron X-radiography study of the fragmentation and refinement of primary intermetallic particles in an Al-35 Cu alloy induced by ultrasonic melt processing, *Acta Mater.* 141 (2017) 142–153, <https://doi.org/10.1016/j.actamat.2017.09.010>.
- [13] F. Chen, Q. Cao, C. Dong, B. Shao, W. Zhai, X. Ma, B. Wei, Ultrasonic polymerization of CuO@PNIPAM and its temperature tuning glucose sensing behavior, *Ultrason. Sonochem.* 49 (2018) 190–195, <https://doi.org/10.1016/j.ulsonch.2018.08.002>.
- [14] S. Raut-Jadhav, D.V. Pinjari, D.R. Saini, S.H. Sonawane, A.B. Pandit, Intensification of degradation of methomyl (carbamate group pesticide) by using the combination of ultrasonic cavitation and process intensifying additives, *Ultrason. Sonochem.* 31 (2016) 135–142, <https://doi.org/10.1016/j.ulsonch.2015.12.015>.
- [15] Y. Iida, J. Lee, T. Kozuka, K. Yasui, A. Towata, T. Tuziuti, Optical cavitation probe using light scattering from bubble clouds, *Ultrason. Sonochem.* 16 (2009) 519–524, <https://doi.org/10.1016/j.ulsonch.2008.12.003>.
- [16] I. Tzanakis, G.S.B. Lebon, D.G. Eskin, K. Pericleous, Investigation of the factors influencing cavitation intensity during the ultrasonic treatment of molten aluminium, *Mater. Des.* 90 (2016) 979–983, <https://doi.org/10.1016/j.matdes.2015.11.010>.
- [17] K.L. Tan, S.H. Yeo, Bubble dynamics and cavitation intensity in milli-scale channels under an ultrasonic horn, *Ultrason. Sonochem.* 58 (2019), 104666, <https://doi.org/10.1016/j.ulsonch.2019.104666>.
- [18] O. Kwon, K.J. Pahk, M.J. Choi, Simultaneous measurements of acoustic emission and sonochemical luminescence for monitoring ultrasonic cavitation, *J. Acoust. Soc. Am.* 149 (2021) 4477–4483, <https://doi.org/10.1121/10.0005136>.
- [19] Z. Liang, G. Zhou, S. Lin, Y. Zhang, H. Yang, Study of low-frequency ultrasonic cavitation fields based on spectral analysis technique, *Ultrasonics* 44 (2006) 115–120, <https://doi.org/10.1016/j.ultras.2005.09.001>.

- [20] C. Li, ChongFu Ying, LiXin Bai, JingJun Deng, The characteristic of cavitation noise and the intensity measurement of hydrodynamic cavitation, *Sci. Sin. Phys. Mech. Astron.* 42 (10) (2012) 987–995.
- [21] V. Grosjean, C. Julcour, O. Louisnard, L. Barthe, Axial acoustic field along a solid-liquid fluidized bed under power ultrasound, *Ultrason. Sonochem.* 56 (2019) 274–283, <https://doi.org/10.1016/j.ultsonch.2019.04.028>.
- [22] M. Khavari, A. Priyadarshi, A. Hurrell, K. Pericleous, D. Eskin, I. Tzanakis, Characterization of shock waves in power ultrasound, *J. Fluid Mech.* 915 (2021), <https://doi.org/10.1017/jfm.2021.186>.
- [23] M. Hodnett, R. Chow, B. Zeqiri, High-frequency acoustic emissions generated by a 20 kHz sonochemical horn processor detected using a novel broadband acoustic sensor: a preliminary study, *Ultrason. Sonochem.* 11 (2004) 441–454, <https://doi.org/10.1016/j.ultsonch.2003.09.002>.
- [24] P. Wu, X. Wang, W. Lin, L. Bai, Acoustic characterization of cavitation intensity: A review, *Ultrason. Sonochem.* 82 (2022), 105878, <https://doi.org/10.1016/j.ultsonch.2021.105878>.
- [25] I. Tzanakis, G.S.B. Lebon, D.G. Eskin, K.A. Pericleous, Characterizing the cavitation development and acoustic spectrum in various liquids, *Ultrason. Sonochem.* 34 (2017) 651–662, <https://doi.org/10.1016/j.ultsonch.2016.06.034>.
- [26] K. Johansen, J.H. Song, P. Prentice, Performance characterisation of a passive cavitation detector optimised for subharmonic periodic shock waves from acoustic cavitation in MHz and sub-MHz ultrasound, *Ultrason. Sonochem.* 43 (2018) 146–155, <https://doi.org/10.1016/j.ultsonch.2018.01.007>.
- [27] J. Frohly, S. Labouret, C. Bruneel, I. Looten-Baquet, R. Torguet, Ultrasonic cavitation monitoring by acoustic noise power measurement, *J. Acoust. Soc. Am.* 108 (2000) 2012–2020, <https://doi.org/10.1121/1.1312360>.
- [28] K. Johnston, C. Tapia-Siles, B. Gerold, M. Postema, S. Cochran, A. Cuschieri, P. Prentice, Periodic shock-emission from acoustically driven cavitation clouds: A source of the subharmonic signal, *Ultrasonics* 54 (2014) 2151–2158, <https://doi.org/10.1016/j.ultras.2014.06.011>.
- [29] T. Matsunaga, K. Ogata, T. Hatayama, K. Shinozaki, M. Yoshida, Effect of acoustic cavitation on ease of infiltration of molten aluminum alloys into carbon fiber bundles using ultrasonic infiltration method, *Compos. Part Appl. Sci. Manuf.* 38 (2007) 771–778, <https://doi.org/10.1016/j.compositesa.2006.09.003>.
- [30] S. Komarov, K. Oda, Y. Ishiwata, N. Dezhkunov, Characterization of acoustic cavitation in water and molten aluminum alloy, *Ultrason. Sonochem.* 20 (2013) 754–761, <https://doi.org/10.1016/j.ultsonch.2012.10.006>.
- [31] I. Tzanakis, M. Hodnett, G.S.B. Lebon, N. Dezhkunov, D.G. Eskin, Calibration and performance assessment of an innovative high-temperature cavitometer, *Sens. Actuators Phys.* 240 (2016) 57–69, <https://doi.org/10.1016/j.sna.2016.01.024>.
- [32] P. Wu, L. Bai, W. Lin, On the definition of cavitation intensity, *Ultrason. Sonochem.* 67 (2020) 105141, <https://doi.org/10.1016/j.ultsonch.2020.105141>.
- [33] Y. Zhao, X. Zhang, Y. Yao, J. Huang, Techniques on ship radiated noise power spectrum feature extraction and realization, *Comput. Meas. Control.* 1 (2010) 554–558, <https://doi.org/10.1109/ICCAE.2010.5451865>.
- [34] N. Srivastava, G.P. Chaudhari, M. Qian, Grain refinement of binary Al-Si, Al-Cu and Al-Ni alloys by ultrasonication, *J. Mater. Process. Technol.* 249 (2017) 367–378, <https://doi.org/10.1016/j.jmatprotec.2017.06.024>.